View metadata, citation and similar papers at core.ac.uk

brought to you by CORE

provided by Repository@USM

SYNTHESIS AND CHARACTERIZATION OF ZnO NANOSTRUCTURES USING PHYSICAL VAPOR DEPOSITION AND ELECTROCHEMICAL DEPOSITION FOR OPTOELECTRONIC APPLICATIONS

By

NADIM KHALID HASSAN

Thesis submitted in fulfillment of the requirements for the degree of Doctor of Philosophy

October 2013

ACKNOWLEDGMENTS

"In the name of ALLAH, The most merciful and the most beneficial"

My foremost thanks go to my supervisor Professor Dr. Md Roslan Hashim for all knowledge and confidence he has given me and for his patience and kindness that he showed toward me. I greatly appreciate his support and helpful suggestions through all the stages of my work.

I would like to express my gratitude to all the members of the N.O.R. LAB at the School of Physics, USM for their generous assistance in the characterizations of the samples.

I offer my sincerest wishes and warmest thanks to all my group members especially Kamaledin Mohammed, and Nima Naderi for their encouragements.

My grateful thanks go to my parents for their prayers, my family members, wife and kids for their patience during my research, and my brothers for their encouragements.

Nadim Khalid Hassan

Penang, Malaysia. 2013

TABLE OF CONTENTS

ACKNOWLEDGMENTS ii

TABLE OF CONTENTS iii

LIST OF FIGURES x

LIST OF TABLES xvi

LIST OF SYMBOLS xix

LIST OF MAJOR ABBREVIATIONS xxi

ABSTRAK xxii

ABSTRACT xxv

CHAPTER 1: INTRODUCTION 1

1.1 Overview of Nanostructures 1

1.2 Problem Statement 3

1.3 Research Objective 3

1.4 Research Originality 4

1.5 Thesis Outline 4

CHAPTER 2: LITERATURE REVIEW AND THEORY 6

2.1 Introduction 6

2.2 Fundamental Properties of ZnO 6

2.3 Overview of ZnO Growth Techniques 8

23.1 Overview of 1D ZnO Growth by VS Method 8

2.3.2 Overview of the 3D ZnO Deposition by ECD Process 11

2.4 Theory of Photoluminescence (PL) and Defects in ZnO 13

2.5 Determination of Out-of-Plane and In-Plane Strains by X-ray Diffraction (XRD) 14

2.6 Theory of Raman Scattering and Determination of Biaxial Stress 16
2.7 Overview of Metal-ZnO-Metal Contact 17
2.7.1 Ohmic Contact on ZnO 18
2.7.2 Schottky Contact on ZnO 18
2.7.3 Mechanism and Operational Parameters of UV-PDs 20
2.7.3.1 Responsivity 21
2.7.3.2 Quantum Efficiency 22
2.7.3.3 Sensitivity 23
2.7.3.4 Rise and Fall Time 23
CHAPTER 3: METHODOLOGY 24
3.1 Introduction 24
3.2 Synthesis of 1D ZnO by PVD Method in a Tube Furnace 24
3.2.1 Wafer Cleaning 24
3.2.2 PVD Furnace 25
3.2.3 Synthesis Conditions of 1D ZnO Nanostructure 25
3.2.3.1 Effect of Reaction Time 26
3.2.3.2 Synthesis of 1D ZnO on Different Substrates 26
3.2.3.3 Synthesis of 1D ZnO at Different Reaction Temperatures 27
3.2.3.4 Synthesis of 1D ZnO nanostructures on SiO_2 Using ZnO Thin Film as Buffer Layer 27
3.3 ECD of 3D ZnO Nanostructures 28
3.3.1 Preparation of Electrolytes 28
3.3.2 Preparation of substrates 28
3.3.3 ECD Cell 29

3.3.4 Synthesis Conditions of ZnO using ECD Technique 29

3.3.4.1 Different Current Densities 30

3.3.4.2 Different $Zn(NO_3)_2.6H_2O$ concentrations 30

3.3.4.3 Different Crystallographic Orientations of the n-Type Si Substrate 30

3.3.4.4 Different Deposition Times 30

3.4 Fabrication and Characterization of Devices 31

3.4.1 Evaporation of Metals 31

3.4.2 Fabrication of MSM UV-PDs 32

3.4.3 Characterization of MSM UV-PDs 33

3.5 Instrumentations 33

3.5.1 SEM and EDX 33

3.5.2 High Resolution (HR)-XRD 34

3.5.3 PL and Raman Measurements 35

CHAPTER 4: GROWTH AND CHARACTRIZATION OF ZnO USING PHYSICAL VAPOR DEPOSITION 36

4.1 Introduction 36

4.2 1D and Tetrapods-like ZnO nanostructures Grown on Si (100) at Different Reaction Time 36

4.2.1 SEM and EDX of PVD ZnO Nanostructures Grown on Si (100) at Different Reaction Time 37

4.2.2 XRD of PVD ZnO Nanostructures Grown on Si (100) at Different Reaction Time 40

4.2.3 Photoluminescence (PL) Characterization of PVD ZnO Nanostructures Grown on Si (100) at Different Reaction Time 41

4.2.4 Raman Analysis of PVD ZnO Nanostructures Grown on Si (100) at Different Reaction Time 43

4.3 Synthesis of High-Quality One-Dimensional ZnO on Different Substrates 45
4.3.1 SEM and EDX of PVD ZnO Nanostructures Grown on Different Substrates 45
4.3.2 XRD of PVD ZnO Nanostructures Grown on Different Substrates 49
4.3.3 Photoluminescence (PL) Characterization of PVD ZnO Nanostructures Grown on Different Substrates 52
4.3.4 Raman Analysis of PVD ZnO Nanostructures Grown on Different Substrates 54
4.4 1D ZnO nanostructures Synthesized on Si (111) at Different Temperature 56
4.4.1 SEM and EDX of PVD ZnO Nanostructures Grown on Si (111) at Different Temperatures 57
4.4.2 X-Ray Studies of PVD 1D ZnO nanostructures Grown on Si (111) at Different Temperatures 59
4.4.3 Photoluminescence (PL) Characterization Grown on Si (111) at Different Temperatures 61
4.4.4 Raman Analysis of PVD ZnO Nanostructures Grown on Si (111) at Different Temperatures 63
4.5 ZnO Thin Film as Buffer Layer to Growth 1D ZnO Nanostructures on SiO_2 65
4.5.1 SEM and EDX of PVD 1D ZnO nanostructures Grown on SiO_2 65
4.5.2 X-Ray Studies of PVD 1D ZnO nanostructures Grown on SiO_2 66
4.5.3 Photoluminescence (PL) Characterization of 1D ZnO nanostructures Grown on SiO_2 67
4.5.4 Raman Analysis of 1D ZnO nanostructures Grown on SiO_2 68
4.6 Metal-Semiconductor-Metal (MSM) UV-Photodetector (UV-PDs) Based on 1D ZnO nanostructures 69
4.6.1 ZnO MSM UV Photodetector with Ohmic Contact 70

4.6.2 ZnO MSM UV Photodetector with Schottky Contact 73

4.7 MSM-UV Photodetector Characteristics Based on the 1D ZnO nanostructures and Nanotetrapods 78

4.8 Summary 84

CHAPTER 5: GROWTH AND CHARACTRIZATION OF ZnO USING ELECTROCHEMICAL DEPOSITION 85

5.1 Introduction 85

5.2 Synthesis of Pyramidal ZnO Nanostructures on Si (100) at Different Current Densities 85

5.2.1 SEM and EDX Analyses of the ECD ZnO Nanostructures Deposited on Si (100) at Different Current Densities 86

5.2.2 X-Ray Studies on ECD ZnO Nanostructures Deposited on Si (100) at Different Current Densities 88

5.2.3 PL Characterization of ECD ZnO Nanostructures Deposited on Si (100) at Different Current Densities 90

5.2.4 Raman Analysis of the ECD ZnO Nanostructures Deposited on Si (100) at Different Current Densities 93

5.3 ECD ZnO Nanostructures Deposited on Si (100) at Different Zinc Nitrate Concentrations 95

5.3.1 SEM Analysis of the ECD ZnO Nanostructures Deposited on Si (100) at Different Zinc Nitrate Concentrations 95

5.3.2 XRD Analysis of the ECD ZnO Nanostructures Deposited on Si (100) at Different Zinc Nitrate Concentrations 97

5.3.3 PL Characterization of the ECD ZnO Nanostructures Deposited on Si (100) at Different Zinc Nitrate Concentrations 100

5.3.4 Raman Spectrum Analysis of the ECD ZnO Nanostructures Deposited on Si (100) at Different Zinc Nitrate Concentrations 102

5.4 ZnO Pyramids and Nanoflakes Deposited on Silicon with Different Crystallographic Orientations 103

5.4.1 SEM and EDX of Analyses of the ECD ZnO Nanostructures 104

Deposited on Si (100) and Si (111)

5.4.2 XRD Analysis of the ECD ZnO Nanostructures Deposited on Si (100) and Si (111) 105

5.4.3 PL Characterization of the ECD ZnO Nanostructures Deposited on Si (100) and Si (111) 107

5.4.4 Raman Spectrum Analysis of the ECD ZnO Nanostructures Deposited on Si (100) and Si (111) 109

5.5 ECD of Flake-Like ZnO Nanostructures on Si (111) at Different Deposition Times 110

5.5.1 SEM and EDX Analyses of the ECD ZnO Nanostructures Deposited on Si (111) at Different Deposition Times 111

5.5.2 XRD Analysis of the ECD ZnO Nanostructures Deposited on Si (111) at Different Deposition Times 113

5.5.3 PL Characterization of the ECD ZnO Nanostructures Deposited on Si (111) at Different Deposition Times 114

5.5.4 Raman Analysis of the ECD ZnO Nanostructures Deposited on Si (111) at Different Deposition Times 117

5.6 MSM UV-PDs Based on the ECD ZnO Nanostructures 118

5.6.1 ZnO MSM UV Photodetector with Ohmic Contact 118

5.6.2 ZnO MSM UV Photodetector with Schottky Contact 122

5.7 MSM-UV Photodetector Characteristics Based on the Size of ZnO Nanoflakes 127

5.8 Comparative study of UV photodetectors based on ZnO nanostructures grown by ECD and PVD on Si (111) 134

5.8.1 Introduction 134

5.8.2 ZnO MSM UV PDs with Ni Contacts 134

5.9 Summary 139

CHAPTER 6: CONCLUSIONS AND FUTURE WORKS 141

6.1 Conclusions 141

6.2 Future Study 143

REFERENCES 144

LIST OF PUBLICATION 157

LIST OF FIGURES

Figure 2.1	Zinc Oxide wurtzite hexagonal structure	6
Figure 2.2	Illustration of the ZnO nanostructure growth via vapor solid mechanism	11
Figure 2.3	Energy levels of defects in ZnO	13
Figure 2.4	Geometrical illustration of Bragg's law	15
Figure 2.5	A UV-detection mechanism of ZnO Rods. (a) Darkness and (b) UV illumination. (c) Energy band diagram upon UV illumination	21
Figure 2.6	Calculation of : Rise time and Fall time	23
Figure 3.1	(a) Tube furnace. (b) Schematic diagram of the setup used for the growth of ZnO nanostructures	25
Figure 3.2	The ECD cell (a) photo (b) schematic diagram	29
Figure 3.3	(a) Thermal evaporator. (b) Schematic diagram of the setup used in metal deposition	31
Figure 3.4	Metal contacts of complete MSM UV-PDs.	32
Figure 3.5	Schematic diagram of scanning electron microscopy (SEM), energy dispersive X-ray (EDX)	34
Figure 3.6	Schematic diagram of high-resolution X-ray diffraction (XRD)	35
Figure 4.1	SEM images and EDX spectra of ZnO nanostructures grown on Si (100) after (a) 30, (b) 60, (c) 90 and (d) 120 min reaction time	38
Figure 4.2	XRD pattern of ZnO nanostructures grown on Si (100) after (a) 30, (b) 60, (c) 90 and (d) 120 min reaction time	40
Figure 4.3	PL spectra of ZnO nanostructures grown on Si (100) after (a) 30, (b) 60, (c) 90 and (d) 120 min. reaction time	42

Figure 4.4	Raman spectra of ZnO nanostructures grown on Si (100) after (a) 30, (b) 60, (c) 90 and (d) 120 min reaction time	44
Figure 4.5	SEM images and EDX spectra of ZnO nanostructures grown on (a) Si (100), (b) Si (111), (c) SiO_2 and (d) Sapphire	47
Figure 4.6	Illustration of the 1D ZnO growth via vapor solid on different substrates	48
Figure 4.7	XRD pattern of ZnO nanostructures grown on after (a) Si (100), (b) Si (111), (c) SiO_2 and (d) Sapphire	50
Figure 4.8	Room temperature PL spectra of the 1D ZnO nanostructures grown on different substrates (a) Si (100), (b) Si (111), (c) SiO_2, and (d) Sapphire	53
Figure 4.9	Typical Raman scattering spectrum of the 1D ZnO nanostructures grown on different substrates (a) Si (100), (b) Si (111), (c) SiO_2, and (d) Sapphire	55
Figure 4.10	SEM images and EDX spectra of the 1D ZnO nanostructures grown on Si (111) at different temperatures (a) 700, (b) 800, (c) 900 and (d) 1000 ^oC	57
Figure 4.11	XRD pattern of the 1D ZnO nanostructures grown on Si (111) at different temperatures (a) 700, (b) 800, (c) 900 and (d) 1000 ^oC	60
Figure 4.12	Room temperature PL spectra of the 1D ZnO nanostructures grown on Si (111) at different temperatures (a) 700, (b) 800, (c) 900 and (d) 1000 ^oC	61
Figure 4.13	Typical Raman scattering spectrum of the 1D ZnO nanostructures grown on Si(111) at different temperatures (a) 700, (b)800 ,(c) 900 and (d) 1000 ^oC	64
Figure 4.14	SEM images of (a) ZnO buffer layer and (b) 1D ZnO nanostructures grown on Si (111)/SiO_2/ZnO substrate	66
Figure 4.15	The XRD pattern of (a) ZnO buffer layer and (b) 1D ZnO nanostructures grown on Si (111)/SiO_2/ZnO substrate	67
Figure 4.16	The PL spectra of (a) ZnO buffer layer and (b) 1D ZnO nanostructures grown on Si (111)/SiO_2/ZnO substrate	68

Figure 4.17	Raman spectrum of (a) ZnO buffer layer and (b) 1D ZnO nanostructures grown on Si (111)/SiO_2/ZnO substrate	69
Figure 4.18	I–V characteristics of the fabricated Al-ZnO-Al on Si (111)/SiO_2/ZnO (UV-PDs) in dark (dark current) and under UV illumination	70
Figure 4.19	The photocurrent time response of the Al-ZnO-Al on Si (111)/SiO_2/ZnO photodetector	71
Figure 4.20	Room temperature responsivity spectra of the Al-ZnO-Al on Si (111)/SiO_2/ZnO photodetector	73
Figure 4.21	I–V characteristics of the fabricated Ag-ZnO-Ag on Si (111)/SiO_2/ZnO (UV-PDs) in dark (dark current) and under UV illumination	74
Figure 4.22	The photocurrent time response of the Ag-ZnO-Ag on Si (111)/SiO_2/ZnO photodetector	75
Figure 4.23	Room temperature responsivity spectra of the Ag-ZnO- Ag on Si (111) /SiO_2/ZnO photodetector	76
Figure 4.24	I–V characteristics of the fabricated (a) Ag/ZnO Rods -Ag, (b) Ag/ZnO TPs –Ag, MSM photodetectors measured in dark UV illumination	79
Figure 4.25	The photocurrent time response of the (a) Ag/ZnO Rods - Ag, (b) Ag/ZnO TPs –Ag, MSM photodetectors	81
Figure 4.26	Room temperature and voltage 5V responsivity spectra of the (a) Ag/ZnO Rods -Ag, (b) Ag/ZnO TPs –Ag, MSM photodiodes	83
Figure 5.1	SEM images of ZnO nanostructures deposited for 90 min at different current densities of (a) 2, (b) 3, (c) 4 mA/cm^2 and (d) the EDX spectra	86
Figure 5.2	XRD pattern of the samples grown at various current densities: (a) 2, (b) 3, and (c) 4 mA/cm^2	89
Figure 5.3	Room-temperature PL spectra of the samples grown at various current densities: (a) 2, (b) 3, and (c) 4 mA/cm^2	91
Figure 5.4	Raman spectra of the samples grown at various current densities: (a) 2, (b) 3, and (c) 4 mA/cm^2	94

Figure 5.5	SEM images of the ZnO nanostructures deposited on Si (100) using different zinc nitrate concentrations: (a) 0.05, (b) 0.075, (c) 0.1, and (d) 0.125 M. (e) EDX spectra	96
Figure 5.6	XRD pattern of the ZnO nanostructures deposited on Si (100) using different zinc nitrate concentrations: (a) 0.05, (b) 0.075, (c) 0.1, and (d) 0.125 M	98
Figure 5.7	PL spectra of the ZnO nanostructures deposited on Si (100) using different zinc nitrate concentrations: (a) 0.05, (b) 0.075, (c) 0.1, and (d) 0.125 M	101
Figure 5.8	Raman spectrum of the ZnO nanostructures deposited on Si (100) using different zinc nitrate concentrations: (a) 0.05, (b) 0.075, (c) 0.1, and (d) 0.125 M	102
Figure 5.9	SEM images and EDX spectra of the ZnO nanostructures deposited on different substrates: (a) Si (111) and (b) Si (100)	104
Figure 5.10	XRD pattern of the ZnO nanostructures deposited for 90 min at 3 mA/cm^2 of current density on different substrates: (a) Si (111) and (b) Si (100)	106
Figure 5.11	PL spectra of the ZnO nanostructures deposited on different substrates: (a) Si (111) and (b) Si (100)	108
Figure 5.12	Raman spectrum of the ZnO nanostructures deposited for 90 min at 3 mA/cm^2 of current density on different substrates: (a) Si (111) and (b) Si (100)	110
Figure 5.13	SEM images of the ZnO nanostructures deposited on Si (111) for (a) 60, (b) 90, (c) 120, and (d) 150 min with (e) EDX spectra of the deposited samples	112
Figure 5.14	XRD pattern of the ZnO nanostructures deposited on Si (111) different deposition times: (a) 60, (b) 90, (c) 120, and (d) 150 min	114
Figure 5.15	PL spectra of the ZnO nanostructures deposited on Si (111) at different deposition times: (a) 60, (b) 90, (c) 120, and (d) 150 min	115
Figure 5.16	Raman spectrum of the ZnO nanostructures deposited on Si	117

(111) at different durations: (a) 60, (b) 90, (c) 120, and (d) 150 min

Figure 5.17 I–V characteristics of the fabricated Al-ECD ZnO-Al (UV-PDs) on (a) Si (111) and (b) Si (100) substrates measured in the dark and under UV illumination 119

Figure 5.18 Photocurrent time responses of PDs based on (a) ZnO nanoflakes/Si (111) and (b) ZnO pyramids/Si (100) 120

Figure 5.19 Room-temperature responsivity spectra of the PD based on (a) ZnO nanoflakes/Si (111) and (b) ZnO pyramids/Si (100) 121

Figure 5.20 I–V characteristics of the fabricated Pd-ECD ZnO-Pd (UV-PDs) on (a) Si (111) and (b) Si (100) substrates measured in the dark and under UV illumination 122

Figure 5.21 Photocurrent time response of Schottky PDs based on (a) ZnO nanoflakes/Si (111) and (b) ZnO pyramids /Si (100) 124

Figure 5.22 Room-temperature responsivity spectra of the PD based on (a) ZnO nanoflakes/Si (111) and (b) ZnO pyramids/Si (100) 126

Figure 5.23 I–V characteristics of the fabricated Ni/ECD ZnO/Ni MSM photodiodes at (a) 90, (b) 120 and (c) 150 min measured in the dark and under UV illumination 128

Figure 5.24 Photocurrent time responses of PDs based on ZnO nanoflakes deposited at (a) 90, (b) 120, and (c) 150 min 130

Figure 5.25 Photocurrent time responses of PDs based on ZnO nanoflakes deposited at (a) 90, (b) 120, and (c) 150 min at a short period time 131

Figure 5.26 Room-temperature responsivity spectra (5 V) of the PD based on ZnO nanoflakes deposited at (a) 90, (b) 120, and (c) 150 min 133

Figure 5.27 I–V characteristics of the fabricated (a) Ni-PVD ZnO-Ni and (b) Ni-ECD ZnO-Ni (UV-PDs) measured in the dark and under UV illumination 135

Figure 5.28 Photocurrent time responses of UV-PDs based on ZnO 137

nanostructures grown on Si (111) by (a) PVD and (b) ECD

Figure 5.29 Photocurrent time responses of UV-PDs based on ZnO nanostructures grown on Si (111) by (a) PVD and (b) ECD at short period time 138

Figure 5.30 Room-temperature responsivity spectra of UV-PDs based on ZnO nanostructures grown on Si (111) by (a) PVD and (b) ECD 139

LIST OF TABLES

Table 2.1	Physical Properties of ZnO	7
Table 2.2	Some of the contact metallization used by researchers for Ohmic contacts	18
Table 2.3	Some of the contact metallization used by researchers for Schottky contacts	19
Table 4.1	The EDX spectra results grown on Si (100) after (a) 30, (b) 60, (c) 90 and (d) 120 min. reaction time	39
Table 4.2	Table 4.2 The FWHM and peak degrees of the XRD planes observed in 1D ZnO nanostructures grown on different substrates (a) Si (100), (b) Si (111), (c) SiO2, and (d) Sapphire samples.	51
Table 4.3	Variation of shift of E2 (High) mode ($\Delta\omega$) and stress (σ) with Si (100), Si (111), SiO_2, and Sapphire substrates	56
Table 4.4	The EDX spectra results of the 1D ZnO nanostructures grown on Si (111) at different temperatures	58
Table 4.5	Lattice parameters (a and c), the lattice spacing (d) and the c/a ratio determined for the prepared ZnO nanowires	61
Table 4.6	Values of measured photoelectrical parameters of Al-ZnO-Al (UV-PDs)	72
Table 4.7	The ideality factor (n), Schottky barrier height (ΦB), dark and photo-current (I) and Series resistance (Rs) measured at 5V	74
Table 4.8	Values of measured photoelectrical parameters of Ag-ZnO-Ag (UV-PDs)	75
Table 4.9	The ideality factor, SBH and photo-current to dark ratio of Ag/ZnO Rods and TPs/Ag PD	80
Table 4.10	Values of responsivity, quantum efficiency and measured time characteristics for three samples	81
Table 4.11	Comparison of the photoresponsivity of different ZnO based photodetector at 5V	84

Table 5.1	EDX spectra results of ZnO nanostructures deposited on Si (100) at different current densities.	87
Table 5.2	Lattice parameters (a and c), in-plane strain (εa), and out-of-plane strain (εc) for the ZnO samples deposited at different current densities	89
Table 5.3	Ratio of Zn to O obtained from the EDX spectra of the ZnO nanostructures deposited on Si (100) using different zinc nitrate concentrations	97
Table 5.4	Lattice parameters (d and c) and out-of-plane strain (εc) determined for the ZnO samples deposited on Si (100) using different zinc nitrate concentrations	99
Table 5.5	Data obtained from XRD of the ZnO nanostructures deposited on different substrates Si (111) and Si (100)	107
Table 5.6	Data obtained from PL of the ZnO nanostructures deposited on different substrates Si (111) and Si (100)	109
Table 5.7	Zn to O ratio obtained from the EDX spectra of the ZnO nanostructures deposited on Si (111) at different deposition times	112
Table 5.8	Wavelength, FWHM, intensity, and NBE/DLE ratio obtained from the PL spectra at room temperature of the ECD ZnO nanostructures on Si (111) at different deposition times	116
Table 5.9	Values of measured photoelectrical parameters of Al-ZnO-Al (UV-PDs)	120
Table 5.10	Ideality factor, SBH, and photo-current to dark ratio of Pd-ZnO-Pd (UV-PDs)	124
Table 5.11	Values of measured photoelectrical parameters of Pd-ZnO-Pd (UV-PDs)	125
Table 5.12	Ideality factor, SBH, and contrast ratio of the Ni-ZnO-Ni (UV-PDs)	129
Table 5.13	Values of responsivity, quantum efficiency, and measured time characteristics of the three samples	132
Table 5.14	Ideality factor, SBH, and contrast ratio of Ni-ZnO-Ni	136

(UV-PDs)
Table 5.15 Values of measured photoelectrical parameters of Ni-ZnO-Ni (UV-PDs) 138

LIST OF SYMBOLS

A	Atomic
A	Contact area
a	Lattice constant in X-axis
ε_a	in-plane strain
A**	Richardson constant
a_o	Lattice constant in X-axis for bulk material
c	Lattice constant in Z-axis
ε_c	Out –of -plane strain
c_o	Lattice constant in Z-axis for bulk material
d	Interplanar spacing of the crystal planes
E_{CB}	Conduction band energy level
E_F	Fermi level of semiconductor
E_{Fm}	Fermi level of metal
E_{gap}	Semiconductor band gap
E_{VB}	Valence band energy level
h	Plank's Constant
I	Electric current
I_d	Dark Current
I_o	Saturation current
I_{ph}	Photo current
k	Boltzmann constant
n	Ideality factor
P	Incidence light power
q	Charge of an electron
R	Responsivity
Rs	Series Resistance
S	Sensitivity
T	Absolute temperature
V	Voltage
W	Weight
Δω	The shift in E_2 (high) mode of Raman spectra
η	Quantum Efficiency

θ	X-ray diffraction angle
λ	Wavelength
ν	Frequency
σ	Lattice Stress
φ_B	Schottky barrier height
φ_m	Metal work function
φ_s	Semiconductor work function
χ	Electron affinity

LIST OF MAJOR ABBREVIATIONS

a. u.	Arbitrary Unit
CB	Conduction band
DLE	Deep-Level-Emission
ECD	Electrochemical deposition
EDX	Energy Dispersive X-ray analysis
eV	Electron volt
FWHM	Full width at half maximum
I-V	Current-Voltage
LO	Longitudinal optic
M	Metal
MOS	Metal Oxide Semiconductors
MS	Metal Semiconductor
MSM	Metal-Semiconductor-Metal
NBE	Near-Band-Edge Emission
nm	Nanometer
PL	Photoluminescence
PVD	Physical Vapor Deposition
R	Responsivity
RCA	Radio Corporation of America
RF	Radio Frequency
SBH	Schottky barrier height
sccm	Standard cubic centimeters per minute
SEM	Scanning Electron Microscopy
TO	Transverse optic
UV	Ultra Violet
VB	Valence Band
XRD	X-Ray Diffraction

SINTESIS DAN PENCIRIAN STRUKTUR NANO ZnO MENGGUNAKAN TEKNIK-TEKNIK PEMENDAPAN WAP FIZIKAL DAN PEMENDAPAN ELEKTRO-KIMIA UNTUK PENGGUNAAN OPTOELEKTRONIK.

ABSTRAK

Nano-struktur ZnO dikembangkan menggunakan teknik-teknik yang mudah untuk membangunkan pengesan foto semikonduktor berasaskan ZnO untuk pengesanan ultra lembayung (UV). Kajian ini menggunakan dua teknik; pertama teknik pemendapan wap fizikal (PVD) dan kedua, teknik pemendapan elektro-kimia (ECD). Dalam proses PVD, wap Zn yang terkondensasi bertindak balas dengan oksigen melalui mekanisme pejal wap dalam relau tiub tiga-zon. Bahan untuk PVD adalah serbuk Zn yang meruap di bawah tiga keadaan tindakbalas yang berlainan. Variasi dalam masa tindakbalas, substrat dan suhu dalam relau didapati mengawal mekanisme pertumbuhan dan morfologi struktur nano. Contohnya, nanorod ZnO yang sejajar telah dicapai ke atas SiO menggunakan lapisan nipis ZnO sebagai lapisan penampan. Ada kemungkinan juga tetrapod nano (TPs) dan wayar nano dibangunkan dengan diameter dan panjang yang berlainan, seperti yang telah disahkan melalui pengimejan SEM.

Pengukuran photolumiscence (PL) pada suhu bilik menunjukkan satu puncak yang dominan berkaitan dengan pancaran berdekatan jalur pada lebih kurang 376nm dengan puncak tambahan berkaitan dengan pancaran jalur hijau pada lebih kurang 520nm. Nisbah pancaran berdekatan pancaran jalur hijau tertinggi nanorod Zn yang tumbuh pada Si(111) boleh terjadi dari pengkristalan tinggi nanostruktur yang difabrikasi. Pengukuran spektra Raman menunjukkan empat puncak yang mana E_2 tinggi menjadi puncak paling dominan. Pertukaran puncak ini dari 437cm^{-1} memberikan maklumat yang tepat tentang tekanan dalam kekisi lapisan ZnO.

ECD pula melibatkan penggunaan dua elektrod dalam sel Teflon yang direka sendiri. Bahan sumber dalam sistem ini adalah nitrat Zn [$Zn(NO_3)_2$].Parameter pemendapan yang berlainan seperti ketumpatan arus, kepekatan elektrolit, bahan substrat dan masa pemendapan telah dikaji sebagai satu kaedah mengawal pertumbuhan dan morfologi pembinaan nano ZnO. Dengan menggunakan teknik ini, kita boleh mengembangkan piramid nano dan flak nano ZnO. Sama seperti struktur nano yang disintesiskan PVD, pengukuran PL pada suhu bilik menunjukkan dua puncak yang bergantung kepada kualiti struktur nano ZnO, satu pancaran berdekatan jalur pada lebih kurang 376nm dengan puncak tambahan yang berkait dengan pancaran jalur hijau pada lebih kurang 520 nm, nisbah pancaran berdekatan jalur hijau tertinggi nanoflak ZnO termendap ke atas Si (111) pada minit ke 90 masa pemendapan boleh terhasil dari pengkristalan tinggi struktur nano yang difabrikasi. Pengukuran spektra Raman juga menunjukkan empat puncak, di mana E_2 tinggi menjadi puncak yang paling dominan. Nilai perubahan yang lebih rendah dalam posisi puncak tinggi E_2 telah didapati dalam nanoflak ZnO yang termendap ke atas Si (111) pada 90 min masa pemendapan, yang menunjukkan bahawa ia berada di bawah tekanan paling rendah dan ia mempunyai penghabluran terbaik.

Alat- alat pengesan foto (PD) yang berasaskan struktur nano ZnO secara fizikal dan elektro-kimia telah dibangunkan. Logam semikonduktor dan logam ZnO PD dengan sentuhan ohmic dan Schottky menggunakan struktur-struktur ZnO yang berlainan juga telah ditunjukkan.Keputusan-keputusan menunjukkan bahawa pengesan Schottky UV berasaskan kepada ZnO Rods yang tumbuh di atas SiO oleh PVD dalam relau mempunyai arus gelap yang rendah kira-kira 0.52 µA, daya sambutan yang tinggi (R) 1.01 A/W, dan masa sambutan yang cepat iaitu 8 ms. Sebaliknya, pengesan UV Schottky berdasarkan kepada ECD nanoflak ZnO tumbuh

di atas Si (111) menunjukkan arus gelap yang rendah kira-kira 1.62 μA, R of 0.12 A/W, dan masa sambutan 50 ms.

SYNTHESIS AND CHARACTERIZATION OF ZnO NANOSTRUCTURES USING PHYSICAL VAPOR DEPOSITION AND ELECTROCHEMICAL DEPOSITION TECHNIQUES FOR OPTOELECTRONIC APPLICATIONS

ABSTRACT

ZnO nanostructures were grown by simple techniques to develop ZnO-based semiconductor photodetectors (PDs) for UV detection. This work employed two techniques, first, physical vapor deposition (PVD) and second, electrochemical deposition (ECD) techniques. In the PVD process, condensed Zn vapor is reacted with oxygen via vapor solid mechanism in three-zone tube furnace. The source material for PVD was pure Zn powder evaporated under different reaction conditions. Variations in the reaction time, substrates, and temperature in the furnace were found to control the growth mechanism and morphology of the ZnO nanostructures. For instance, high quality 1D ZnO nanostructures (Rods) were achieved on SiO_2 using ZnO thin film as a buffer layer. Also, it was possible to grow tetrapods-like ZnO (TPs) and nanowires with different diameters and lengths as confirmed via SEM imaging. Photoluminescence (PL) measurements at room temperature showed a dominant peak related to a near-band-edge emission at approximately 376 nm with an additional peak related to green-band emission at approximately 520 nm.The highest near-band emission to green band emission ratio of 1D ZnO nanostructures grown on Si(111) could result from the high crystallinity of the fabricated nanostructure. Raman spectra measurements show four peaks, of which E_2 high was the dominant peak. The shift in this dominant peak from 437 cm^{-1} provided accurate information of the stress in the ZnO film lattice.

The ECD, on the other hand, involves the use of two electrodes in a homemade Teflon cell. The source material in this system was Zn nitrate [$Zn(NO_3)_2$]. Different deposition parameters, such as current density, electrolyte

concentration, substrate material, and deposition time were investigated as means to control the growth and morphology of the ZnO nanostructures. Using this technique, it was possible to grow ZnO pyramids and nanoflakes. Similar to the PVD-synthesized nanostructures, the PL measurements at room temperature showed two peaks that were dependent on the quality of the ZnO nanostructure, a near-band-edge emission at approximately 376 nm with an additional peak related to green-band emission at approximately 520 nm. The highest near-band emission to green band emission ratio of ZnO nanoflakes deposited on Si (111) at 90 min deposition time could result from the high crystallinity of the fabricated nanostructure. Also, the Raman spectra measurements show four peaks, of which E_2 high was the dominant peak. The lowest shift value in the E_2 high peak position was found in the ZnO nanoflakes deposited on Si (111) at 90 min deposition time, which indicates that it was under the lowest stress and it has the best crystallinity.

UV photodetector (PD) devices based on the physically and electrochemically deposited ZnO nanostructure were developed. Metal-semiconductor-metal ZnO PDs with ohmic and Schottky contacts using different structures of ZnO were also demonstrated. The results showed that the Schottky UV photodetector based on ZnO Rods grown on SiO_2 by PVD in the furnace had low dark current of approximately 0.52 µA, high responsivity (R) of 1.01 A/W, and fast response time of 8 ms. In contrast, the Schottky UV photodetector based on ECD ZnO nanoflakes grown on Si (111) showed low dark current of approximately1.62 µA, R of 0.12 A/W, and response time of 50 ms.

CHAPTER 1: INTRODUCTION

1.1 Overview of Nanostructures

At present, the II-VI semiconductor materials such as ZnO, CdSe ,Cds, CdTe, ZnSe, ZnS and ZnTe have attracted considerable attention due to their promising semiconductor devices applications such as solar cells, photo resistors ,blue lasers and blue LEDs. The emphasis on the II-VI semiconductor materials is inspired by the absence of semiconductor materials that satisfy profitable requirements for blue, green, and UV lasers and light-emitting devices in foregoing years covering the UV spectral ranges.

Among the II-VI semiconductor materials, Zinc oxide (ZnO), has received considerable attention because of its physical and optical properties. ZnO has a stable wurtzite structure, direct bandgap (3.37 eV) and large excitation binding energy (60 meV) at room temperature. ZnO also produces strong emissions even at room temperature, enabling the detection of UV emissions at very high efficiencies by using ZnO-based optical devices [1]. This property is useful to fabricate UV photodetector devices based on ZnO nanostructures. Therefore, the synthesis of ZnO materials has received attention because these materials have exceptional semiconducting properties and exhibit physical and chemical stabilities. These materials are also abundant and cheap, requiring environmentally friendly and simple fabrication process.

Low-dimensional semiconductor nanostructures have become the focus of many fundamental and applied research activities. Improvements of optical

properties have resulted from surface and quantum effects with a decrease in size. Nanoscale of semiconductor materials attracting wide attention owing to their unique physical and chemical properties which are largely dissimilar from that of their bulk phases, improve these properties will in turn enhance their performance in detecting and optoelectronics devices , its characteristics are terrifically distinct from their bulk and are completely new kind of material. The resultant structures often have dimensions in 1nm to 100 nm range. Various sizes lead to various band gaps, absorptions and emissions.

The characteristics of the materials such as electronic, magnetic, optical, and structural can be adapted through the alteration on the shapes and sizes of the material structures. The influence of changes in shapes and sizes of nanostructure material on its characteristics is still under consideration.

Researchers have continuously focused on the synthesis, characterization, and fabrication of ZnO nanodevices because these materials exhibit high performance. Various approaches such as chemical and physical vapor deposition (CVD and PVD respectively), electrochemical deposition (ECD), and microwave-assisted chemical bath deposition are currently applied to produce ZnO nanostructure effectively [1-7].

To date, II–VI (ZnO) semiconductors have received great attention because of their promising device applications in electronics and optoelectronics operating in blue and UV regions of the light spectrum. These semiconductors have a wide band gap that causes such materials to become intrinsic at a much higher temperature than other materials, such as Ge, Si, and GaAs. In other words, intrinsic carrier concentration at any given temperature decreases exponentially with band gap. Therefore, ZnO is attractive for high-temperature applications.

1.2 Problem Statement

The size and dimensionality of the nanostructure is very important as it helps to increase the radiative recombination thereby enhancing the material optical properties [3]. The crystalline morphology, orientation and surface architecture of nanostructures can be well controlled during the preparation processes. The applications of ZnO nanostructures require not only crystalline with the aforementioned characteristics, but also crystals with improved optical and electronic properties. This work employed two well known simple techniques to grow ZnO nanostructures are PVD and ECD. Unfortunately, ZnO nanostructures grown via PVD show poor crystallization and difficulty to control size dimensionality particularly on Si and SiO_2 substrates with large lattice mismatch and different crystalline structures in comparison with ZnO. Hence, it is still a challenge to achieve high quality ZnO nanostructures with low level of defect

The growth parameters of 1D and 3D ZnO nanostructures will be chosen in order to develop high quality ZnO nanostructures to be used in UV-PDs.

1.3 Research Objectives

The main objectives of this study can be summarized as follows:

1. To realize the size and dimensionality controllable growth of the 1D ZnO nanostructures via PVD.
2. To determine the best growth conditions to produce high-quality 3D ZnO nanostructures via ECD.
3. To study the suitability of the grown samples UV- photodetectors.

1.4 Research Originality

The originality of the study is described as follows:

1. Determination of growth parameters to control the size and dimensionality of the fabricated ZnO nanostructures using PVD and ECD.
2. High-quality of 1D ZnO nanostructure arrays on SiO_2 covered by ZnO buffer layer
3. Growth at room temperature with low level of defects of 3D ZnO nanostructures (such as nanoflakes and pyramids).
4. The UV-PDs characteristics based on ZnO nanostructures grown by PVD and ECD.

1.5 Thesis Outline

Chapter 1 presents a brief introduction to the ZnO nanostructure and growth techniques. **Chapter 2** provides a literature review and theoretical background of ZnO synthesized by PVD and ECD. Formation mechanisms and the basic principles of UV-PD devices are also discussed. **Chapter 3** describes the experimental procedures and instrumentation which was used in this study.

Chapter 4 discusses the synthesis and characterization of 1D ZnO by PVD using a tube furnace with different growth parameters and UV-PD application based on 1D ZnO nanostructures grown on SiO_2 using Ohmic and Schottky contacts. This chapter also presents the difference between UV-PDs based on ZnO (nanorods and nanotetrapods). **Chapter 5** discusses the synthesis and characterization of 3D ZnO by ECD with different growth parameters and UV-PD application based on ZnO nanoflakes and pyramids grown on Si using Ohmic and Schottky contacts. This

chapter also presents the difference between UV-PDs based on ZnO nanoflakes with different sizes. The difference between the performances of UV-PDs fabricated on optimal ZnO by using each method was also discussed. Some conclusive remarks and some suggestions for further research are presented in **Chapter 6.**

CHAPTER 2: LITERATURE REVIEW AND THEORY

2.1 Introduction

Chapter 2 presents the fundamental properties in addition to the theories of the synthesis and device applications of ZnO nanostructures, such as nanorods, nanotetrapods, pyramids, and nanoflakes, as well as literature review. This chapter starts with fundamental properties of ZnO. Then brief explanation of the formation mechanism of 1D ZnO by VS as the specific PVD. The fundamental principles of ECD, the mechanism of 3D ZnO formation, and the fundamental theories of metal-semiconductor contacts are addressed. Furthermore, the basic principles of MSM UV-PDs fabricated in this study are briefly described.

2.2 Fundamental Properties of ZnO

ZnO crystallizes in a wurtzite form in addition to other forms, such as zinc blend and cubic rock salt, at room temperature and ambient pressure. Hexagonal wurtzite is one of the most stable forms at ambient temperature and pressure

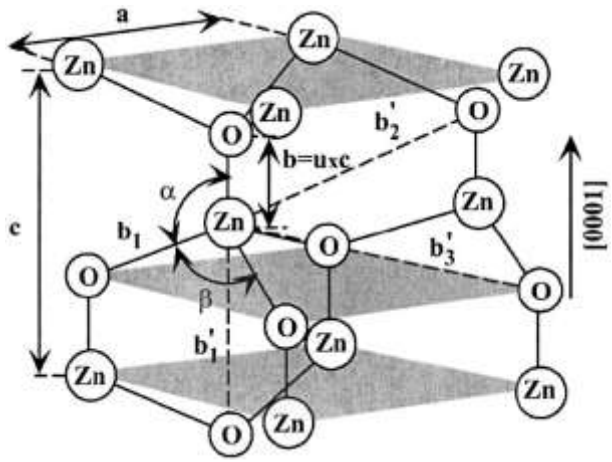

Figure 2.1 Zinc Oxide wurtzite hexagonal structure [8]

This hexagonal form is characterized by two sub-lattices of Zn^{+2} and O^{-2} comprising the alternating basal planes (Fig.2.1). Lattice constants of a unit cell have a c/a proportion of 1.602. The zinc to oxygen coordination number is four where four anions encircle the cations at the tetrahedron corners and vice versa. Table 2.1 shows the properties of wurtzite ZnO.

Table 2.1 Physical Properties of ZnO [9].

Property	Value
Crystal structures stable phase at 300 K	Wurtzite
Lattice parameters at 300 K	
a_o	0.32495 nm
c_o	0.52069 nm
$a_{o/} c_o$	1.60
Density	5.606 g/cm^3
Melting point	1975 ^{o} C
Static dielectric constant	8.656
Refractive index	2.008, 2.029
Energy gap	3.37 eV, direct
Intrinsic carrier concentration (percm^3)	10 ^{16} to 10 ^{20}
Exciton binding energy	60 meV
Electron effective mass	0.24 m_o
Typical defects	Zinc interstitials, Oxygen vacancies, zinc vacancies, complexes

Lots of semiconductors characteristics are identified depending on the crystalline structures of these semiconductors. As previously mentioned, wurtzite is a common crystal structure of ZnO. Although rock salt or zinc-blend structure can also be used relying on growth conditions and kinds of substrates, wurtzite is, thermodynamically stable in ambient conditions. Given that the growth processes of

wurtzite are easier and cheaper than those of cubic structures, studies have focused on the wurtzite crystal phase. Hexagonal structures are stable and can be grown on various substrates such as sapphire [10-12].

2.3 Overview of ZnO Growth Techniques

In recent years, numerous efforts have been devoted to fabricate 1D and 3D ZnO nanostructures by using various methods, such as sol-gel [13], CVD [14, 15] , sputtering[16, 17], pulsed-laser deposition [18],and vapor-phase transport process [19-23].

Vapor transport process is an important approach to grow aligned and uniform ZnO with various nanostructures, such as nanowires, nanorods, and nanotubes, which offer a broad range of technological applications. In addition, the search for easily controllable techniques to fabricate these nanostructures has led to the implementation of a chemically based technique known as ECD [24, 25].

An appropriate Si substrate has several advantages, such as low cost and availability of large substrate dimension in addition to that Si has acceptable value of thermal conductivity. This study focused on the use of VS as the specific PVD and ECD techniques. Such techniques are cost effective for large-scale production and deposition on different substrates because of high and low temperatures involved.

2.3.1 Overview of 1D ZnO Growth by VS Method

Sea urchin-like ZnO nanowires were grown on Si (100) substrates via oxidation of metallic Zn powder at 600 °C [20, 26]**.** and pretreated under H_2 and N_2 flows with Si (100) at 500 °C to 650 °C for 30 min to 120 min (H_2 and N_2,

respectively) [27]. 1D ZnO nanostructures were synthesized by a VS growth mechanism, in which metallic Zn powder and oxygen gas were used as sources. Metallic Zn powder was rapidly heated at a temperature range of 500 °C to 620 °C under N_2 flow [15]. ZnO nanowires were formed by thermal evaporation in a horizontal tube furnace. Evaporation was performed in a reactor for 0.5 h to 2.0 h at 700, 800, 900, and 1000 °C. In this study, the shape of nanostructures changed from rod to wire and then to needle as temperature increased [28]. ZnO nanowires were grown on Si (100) substrates by subjecting metallic Zn powder to thermal evaporation via VS method. The substrate was pretreated under N_2 and H_2 environments at 500 °C for 20 min and at 550 °C to 650 °C for 1 h [21]. ZnO nanospheres and micro-sized hollow spheres/cages were prepared on two different substrates, namely, Si (100) and steel alloy, by VS method [29]. Javelin-like 1D ZnO nanostructures were successfully synthesized using pure Zn PVD on a copper foil by thermal evaporation at 500 °C [22]. PVD was also used to synthesize macro-scale ZnO nanonails on Si without any catalyst. Synthesized ZnO nanonails grew vertically on the substrate; the temperature in the center of the tube increased at a constant rate of 25 °C/min from room temperature to reaction temperature (700 °C) and then remained constant for 90 min [30]. Thermal evaporation was performed to grow various ZnO nanostructures in a single reactor furnace as presented in a previous study [31]. Previous studies also described the syntheses of hollow spheres with club-shaped 1D ZnO nanostructures by PVD [32] and star-like ZnO nanostructures by thermal evaporation [33]. ZnO nanonails were produced with controllable morphology by using an evaporation method [34]. Tetrapod-shaped ZnO nanostructure was formed via oxidation of Zn powder at temperatures higher than 930 °C in air [35]. Hammer-shaped ZnO was synthesized on Si [36]. The growth

mechanism of ZnO on a substrate in a tube furnace does not involve the use of a metal catalyst. Sekar et al, grew polycrystalline ZnO nanowires Si (100) using a rapid thermal reactor at 600 C [37]. Peng et al [38], used the thermal evaporation method to grow ZnO in bulk quantity through evaporation of Zn in tube furnace under O_2 flow. The formed ZnO nanotetrapods showed a low intensity of UV emission at 383nm and a strong green emission at 495 nm at room temperature that were related to the high level of defects. K.M.K. Srivatsa et al [39], grew high density of 1D ZnO nanostructures on Si and sapphire. The fabricated 1D ZnO nanostructures showed a weak intensity in the UV emission at 385 and abroad green emission at 490 nm in addition the grown ZnO showed a very weak E_2 High intensity in Raman spectra indicated the low quality of the grown 1D ZnO nanostructures. Nanostructures have been formed via a VS mechanism with two stages: metal nucleation and growth of the nanostructure. Nucleation involves the agglomeration of atoms or molecules to form the first grain of the extended solid crystal (Fig.2.2). During heating, an increase in temperature causes Zn powders to melt, evaporate, and deposit on substrates under N_2 gas flow. Given that the temperature of the substrate is higher than the melting point of Zn, Zn atoms aggregate to form Zn droplets. These droplets then react with oxygen to form ZnO nuclei by a simple chemical reaction [22]:

$$2Zn\ (g) + O_2\ (g) \rightarrow 2ZnO\ (g) \qquad (2.1)$$

Zn vapor and ZnO are transported as O_2 flows to the substrates. As heating continues under gas flow, more ZnO molecules are absorbed on Zn droplets to form ZnO.

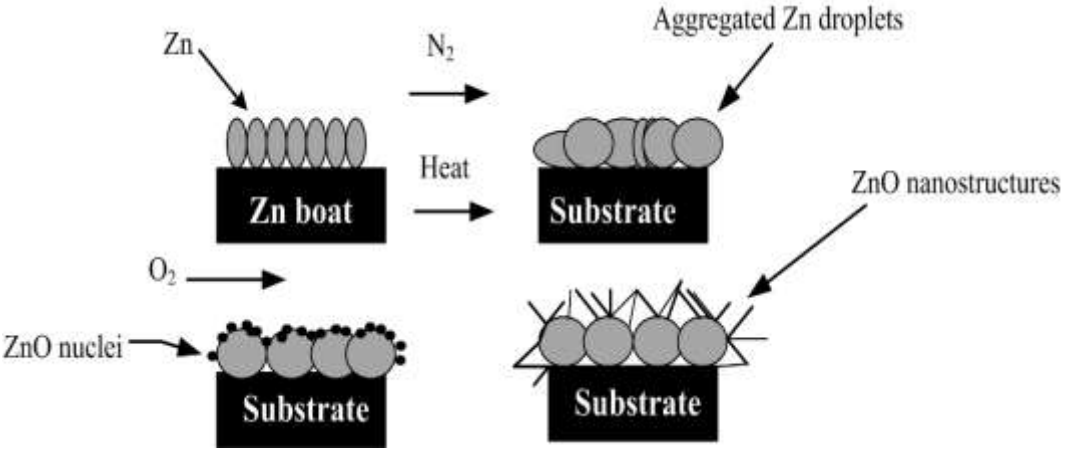

Figure 2.2 Illustration of the ZnO nanostructure growth via vapor solid mechanism

Therefore, Zn droplets have an important function as a source in nanowires formation and as a point at which ZnO branches out to form another structure such as tetrapods or where ZnO molecules are absorbed on the substrate to form new nuclei.

2.3.2 Overview of the 3D ZnO Deposition by ECD Process

In contrast to other techniques, ECD provides several advantages such as controllable the thickness and the morphology of the deposited films by growth conditions, high deposition rate, low-cost experimental setup, and low-temperature process as previously noted. Izaki and Omi [24] as well as Peulon and Lincot [25] first reported the preparation of ZnO films (ECD). Their investigations have prompted other researchers to investigate ZnO growth via ECD and improve the crystal quality as well as electrical and physical properties of ZnO nanostructures.

Studies on the development of ZnO growth using ECD have been continued. The effect of ECD conditions on the properties of ZnO polycrystalline thin film deposited by ECD on ITO substrate has been reported [40]. ZnO thin film is also electrochemically deposited on ITO glass substrates at different deposition times by Gao et al.[1].

A classical three-electrode electrochemical cell was used to grow ZnO nanowires [41]. ZnO thin films were fabricated by ECD at different deposition times, increased deposition time produced smaller band gap energies [42]. ZnO nanowires were electrodeposited on conducting glass from $ZnCl_2$, and $ZnCl_2$ concentration is a major parameter used to control the dimensions of ZnO nanowires [43]. 1D ZnO nanostructures were grown on ZnO seed layer-coated ITO substrate by ECD technique, and the effects of the seed layers on the structures and properties of ZnO nanorod arrays were discussed [44]. 1D ZnO nanostructures and nanodisks were formed on ITO-coated glass substrates using ECD method. The effect of zinc nitrate concentration on the structural and optical properties of the deposited ZnO nanostructures was investigated [45]. Hollow ZnO nanospheres were fabricated at a large scale according to a one-step ECD method at room temperature [46]. The evolution of ZnO nanostructure morphology from nanorods to nanosheets was observed at different concentrations of zinc nitrate electrolyte [47].

The effect of $ZnCl_2$ concentration on the growth of ZnO thin films prepared by ECD on Zn/Si substrates was also reported [48]. Micro-sized ZnO flakes were synthesized by ECD [49] , and nanoporous ZnO thin films were prepared on Ti substrate by ECD method [50]. In this study, zinc nitrate $Zn(NO_3)_2 \cdot 6H_2O$ solution was selected for Electrodeposition of ZnO. As zinc nitrate dissolves in water, under the applied electric field the possible reactions that take place in the cell are expressed as follows [47, 51-54]:

(a) Dissociation $Zn(NO_3)_2 \rightarrow Zn^{2+} + 2NO_3^{1-}$ (2.2)

(b) Hydrolysis $NO_3^- + H_2O + 2e^- \rightarrow NO_2^- + 2OH^-$ (2.3)

(c) Interaction with (OH^-) at the cathode $Zn^{2+} + 2OH^{1-} \leftrightarrow Zn(OH)_2$ (2.4)

(d) Dehydration of the hydroxide $Zn(OH)_2 \rightarrow ZnO + H_2O$ (2.5)

Eqs. (2.4) and (2.5) occur because of the high solubility of ZnO.

2.4 Theory of Photoluminescence (PL) and Defects in ZnO

Various defects can be introduced during the growth process. Thus, the behavior of these defects in ZnO should be understood. PL properties of ZnO are affected by extrinsic and intrinsic defects. ZnO has donor and acceptor energy levels below the conduction band and above the valance band; these energy levels result in near-band edge emissions. In addition, ZnO has deep energy levels in the band gap with different energies, which release deep level emissions (DLE) in the whole visible region from 400 nm to750 nm (figure 2.3).

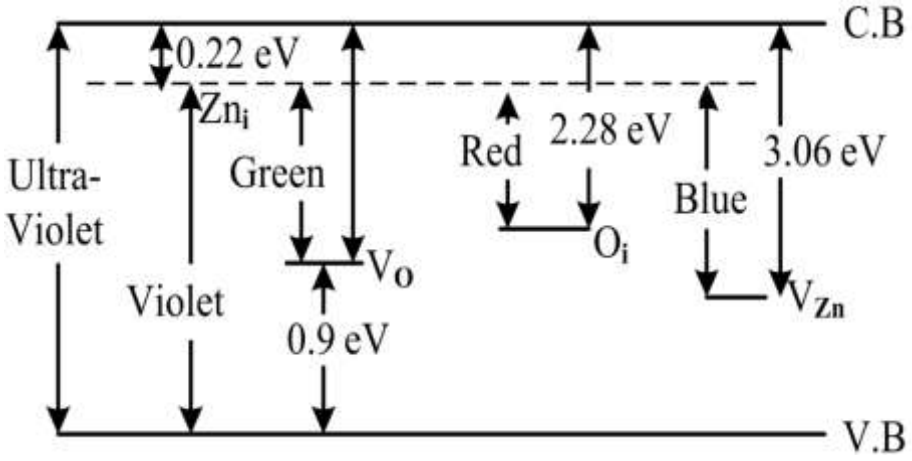

Figure 2.3 Energy levels of defects in ZnO [55].

These levels are intrinsic atoms resulting from defects. The DLE band in ZnO is formed because of different intrinsic defects, such as oxygen vacancies (V_O) and zinc vacancies (V_{Zn}), which are the two most common intrinsic defects, in the crystal structure of ZnO, the vacancy defects are formed when an atom is missing in the crystal and it is denoted by V, zinc vacancies (V_{Zn}) suggested by many researchers to

be the source of the green emission appeared at 2.4 - 2.6 eV below the conduction band in ZnO.[56-64]. Other defects include oxygen interstitial (O_i) [65], zinc interstitial (Zn_i), [66, 67] are not stable at room temperature [68, 69], oxygen anti-site (O_{Zn}), and zinc anti-site (Zn_O) [70]. The interstitial defects are formed when an atom occupying an interstitial site between the normal sites in the crystal structure. The zinc interstitial defects are normally located at 0.22 eV below the conduction band and play vital role in the visible emissions in ZnO by recombination between Zn_i. Oxygen interstitials defects are normally located at 2.28 eV below the conduction band and are responsible for the orange-red emissions in ZnO. Many researchers also suggested oxygen vacancies as the source of green emission in ZnO [62-64], single-ionized V_O in ZnO produces green emission in ZnO. V_O has lower formation energy than Zn_i and dominates in Zn-rich growth conditions. The red luminescence from ZnO is caused by doubly ionized V_O [71].

2.5 Determination of Out-of-Plane and In-Plane Strains by X-ray Diffraction (XRD)

XRD is a useful tool to identify crystal structures of materials. As incident X-rays on ZnO films interact with electrons in atoms, diffracted waves from these different atoms can interfere with each other (Fig. 2.4)

The diffraction condition is expressed according to Bragg's law:

$$2d\sin\theta = n\lambda \tag{2.6}$$

where λ is the wavelength of X-ray, θ is the scattering angle, and n is an integer representing the order of the diffraction peak.

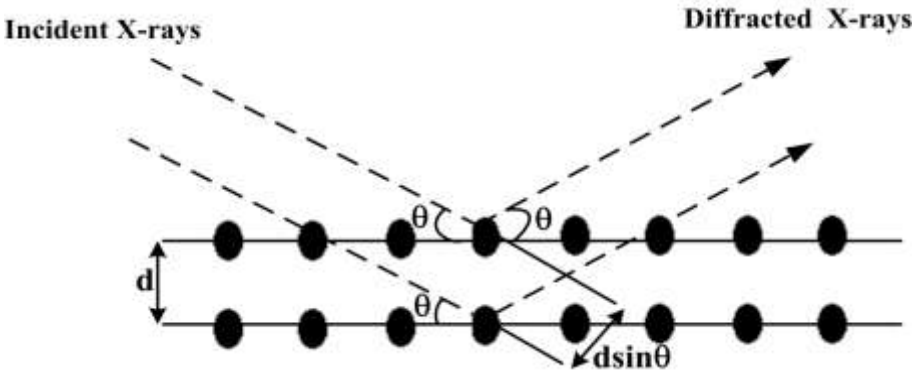

Figure 2.4 Geometrical illustration of Bragg's law

The *d*-spacing equation of a hexagonal lattice is expressed as follows [72-74].

$$\frac{1}{d^2} = \frac{4}{3}\left(\frac{h^2 + hk + k^2}{a^2}\right) + \frac{l^2}{c^2} \tag{2.7}$$

The lattice constants "a" and "c" of the wurtzite structure of ZnO can be calculated using the following relations [75-77]:

$$a = \sqrt{\frac{1}{3}}\frac{\lambda}{\sin\theta} \tag{2.8}$$

$$c = \frac{\lambda}{\sin\theta} \tag{2.9}$$

Thus, out-of-plane and in-plane strains along the *c*- and *a*-axes in the ZnO film can be calculated according to the following equation [78, 79]:

$$\varepsilon_a = \frac{a - a_o}{a_o} \tag{2.10}$$

$$\varepsilon_c = \frac{c - c_o}{c_o} \tag{2.11}$$

where c and a are the calculated lattice parameters (a_o = 3.249 Å and c_o = 5.2067Å are the corresponding unstrained values). The positive values of ε_a and ε_c denote tensile strain, whereas the negative values denote compressive strain.

The amount of residual stress σ in ZnO thin film is derived according to the following equation [77, 80]:

$$\sigma = -233 \times \frac{c - c_o}{c_o}, \text{ i.e. } \sigma = -233 \times \varepsilon_c \tag{2.12}$$

where c is the lattice parameter of the c-axis of the ZnO films and c_o is the lattice parameter of the unstrained ZnO.

2.6 Theory of Raman Scattering and Determination of Biaxial Stress

Raman scattering spectroscopy is an effective technique to estimate the crystallinity of materials. Incident laser light interacts with phonons or other excitations in the film, thereby shifting the energy of the laser photons up or down. This shift in energy provides information about the phonon modes in the system. Raman signals are very sensitive to crystal structures and to the defects in these crystal structures [27, 81-83]. The observed phonon frequencies in the Raman spectra of ZnO are as follows [84]. E_2(high)=437 cm^{-1}, E_2(low)=101 cm^{-1}, A_1 (TO) =380 cm^{-1}, A_1(LO)=574 cm^{-1}, E_1(TO)= 407 cm^{-1} and E_1(LO)=583 cm^{-1}, respectively.

The peak of E_2 (high) for ZnO nanostructures represents the Raman active optical phonon mode. The shift in E_2 (high) mode indicates stress. The relation between stress and E_2 (high) mode shift can be written as follows [83, 85]:

$$\Delta\omega(cm^{-1}) = 4.4\sigma \text{ (GPa)} \tag{2.13}$$

where Δω is the shift in E_2 (high) mode in cm^{-1} and σ is the stress of ZnO structure in GPa. Under compressive stress, E_2 (high) shifts to values higher than 437 cm^{-1}. Under tensile stress, E_2 (high) shifts to values lower than 437 cm^{-1}.The peak of E_2H–E_2L at approximately 330 cm^{-1} could be assigned to the second-order Raman spectrum arising from zone-boundary phonons, and the peak at 561 cm^{-1} is contributed by an E_1 (LO) mode of ZnO associated with oxygen deficiency [86]. The intensity of E_1 mode indicates the level of defects in the ZnO nanostructure. Stronger E_2H mode and lower E_1 (LO) mode indicate a lower V_O.

2.7 Overview of Metal-ZnO-Metal Contact

The metal-semiconductor interface forms two types of contacts, namely, Ohmic and Schottky. An Ohmic contact follows Ohm's law, indicating that the current-voltage relation should be linear. The contact resistance should be very low to produce a negligible decrease in voltage across this contact and a negligible decrease in power**.** Schottky contact or rectifying contact allows high amounts of current to flow in one direction at a low voltage. High barrier height is essential to produce rectifying effects. Ohmic or Schottky contact forms depending on the metal (ϕ_m) and semiconductor work (ϕ_s) functions. Work function is the minimum amount of energy required to remove an electron from the surface of a metal. In theory, Ohmic contact is formed on an *n*-type semiconductor when $\phi_m < \phi_s$ and Schottky contact is formed when $\phi_m > \phi_s$. The semiconductor work function is equal to the sum of the electron affinity (χ_s) and the energy difference between the bottom of the conduction band and Fermi energy (E_F) and, that is, $\phi_s = \chi_s + (E_c - E_F)$. Considering these factors, the selected metals have work functions almost similar to the work function of ZnO as Ohmic and Schottky contacts.

2.7.1 Ohmic Contact on ZnO

High performance UV-PDs based on ZnO can be obtained by a good Ohmic contact with low resistance, thermal stability, and reliability, and these factors can be attained by surface treatment, doping, and metal selection [87]. Various metallization processes for Ohmic contacts on ZnO have been investigated. Table 2.2 summarizes some of the common contact metallization used by researchers for Ohmic contacts.

Table 2.2 Some of the contact metallization used by researchers for Ohmic contacts

Metallization	Dark current (μA)	Photocurrent (mA)	Responsivity at 5 V (A/W)	Reference
Al	200	2.5	1410	[88]
Al	38	0. 882	18	[89]
Al	28	0. 81	406	[90]
Au	18	0.058	68	[87]

2.7.2 Schottky Contact on ZnO

Current flows non-linearly across a metal-semiconductor contact because of a potential barrier generated from the presence of a stable space-charge layer (depletion layer). A potential barrier is present between a metal and a semiconductor when these materials come in contact with each other. This barrier prevents carriers (electrons and holes) from passing from one side to the other. Very few carriers have enough energy to cross or tunnel the barrier and move to the other material. The barrier height changes by either increasing or decreasing in size from the semiconductor side when the junction is under bias voltage.

Table 2.3 Some of the common contact metallization used by researchers for Schottky contacts.

Metallization	Ideality factor(n)	φ_B (eV)	Reference
Ni	-	0.675	[91]
Pd	1.03	0. 83	[92]
Pt	1.51	0. 79	[93]
Pd	2	0.55	[94]
Pt	2	0.55	[94]
Au	1.4	0.71	[94]
Ag	1.2	0.78	[94]

The barrier height does not change from the metal side although the bias voltage is changed. A junction is called a Schottky barrier or a rectifying contact when the junction conducts for one bias polarity and does not conduct for other polarities.

2.7.2.1 Calculation of Barrier Heights and Ideality Factor

An effective Schottky barrier height (SBH) can be found from I–V measurements by assuming that the mechanism of current flow is governed by thermionic emission conditions, which is given by [95-98]**:**

$$I = I_o\left[\exp\left(\frac{qV}{nkT}\right)-1\right] \tag{2.14}$$

where V is the voltage across the diode, n is the ideality factor, k is the Boltzmann constant, and I_o is the saturation current expressed as follow [95, 97]:

$$I_o = AA^{**}T^2 \exp\left[\frac{-q\Phi_{Bo}}{kT}\right] \quad (2.15)$$

where q is the electron charge, T is the temperature in Kelvin, A is the contact area (1.5×10^{-4} cm^2), Φ_{Bo} is the SBH and A^{**} is the effective Richardson constant. For ZnO, A^{**} = 32 A cm^{-2} K^{-2}. The plot of *ln I* vs. *V* shows a straight line and the slope of this line is equal to $q/(nkT)$ in which the ideality factor (n) can be found, and the intercept of y-axis yields I_o, in which barrier height, φ_B, can be obtained using Eq. (2.15). Series resistance (R_S) can be estimated from the I–V characteristics of the diode at a high forward bias as follows [99]:

$$R_s = \left(\frac{\partial I}{\partial V}\right)^{-1} \quad (2.16)$$

2.7.3 Mechanism and Operational Parameters of UV-PDs

Considering that ZnO is an *n*-type semiconductor, surface oxygen participates in the mechanism of UV detection by ZnO nanostructures (figure 2.5). After ZnO-based UV-PD is placed in the dark, oxygen molecules adsorb on the surface, extracting free electrons from *n*-type ZnO. This adsorption creates a depletion layer with low conductivity near the ZnO nanostructure surface [100-105]:

$$O_2(g) + e^- \rightarrow O_2^- \quad \text{(surface)} \quad (2.17)$$

$$O_2(g) + 2e^- \rightarrow O_2^{2-} \text{ (surface)} \quad (2.18)$$

After PD is illuminated with UV light, electron–hole pairs (e^-- h^+) are generated. The electric field formed in the depletion region pushes the holes toward the surface of the ZnO nanostructure, leaving behind the electrons

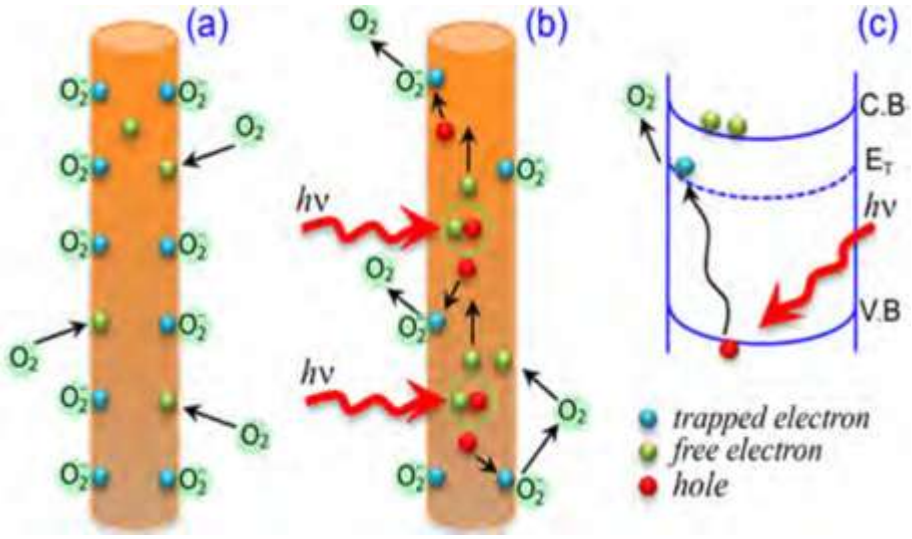

Figure 2.5 A UV-detection mechanism of ZnO Rods. (a) Darkness and (b) UV illumination. (c) Energy band diagram upon UV illumination [106].

These holes reach the surface and recombine with electrons from adsorbed oxygen ions, thereby releasing oxygen atoms from the surface [100-102, 107-109]:

$$h\nu \rightarrow e^{-} + h^{+} \tag{2.19}$$

$$O_2^{-}(\text{surface}) + h^{+} \rightarrow O_2(\text{g}) \tag{2.20}$$

$$O_2^{2-}(\text{surface}) + 2h^{+} \rightarrow O_2(\text{g}) \tag{2.21}$$

This process results in an increase in electron concentration in ZnO nanostructure, thereby increasing conductivity.

2.7.3.1 Responsivity

Responsivity (*R*) refers to the ratio of device photocurrent to incident optical power. *R* is another performance metric used to characterize photodetectors and can be expressed as follows [98, 110-113] :

$$R = \frac{I_{ph}}{P} \tag{2.22}$$

where I_{ph} and P are the photocurrent and the incident optical power on the device respectively. I_{ph} depends on absorption and current collection efficiency. R increases linearly with wavelength for a given value of quantum efficiency.

2.7.3.2 Quantum Efficiency

Quantum efficiency (η) of a photodetector can be described as the number of carriers collected to create I_{ph} produced per number of incident photons. η can be calculated by determining the spectral response based on the following equation [90, 107, 114-117] :

$$R = \frac{\eta q}{h\nu} = \frac{\eta\lambda(\mu m)}{1.24} \tag{2.23}$$

$$\eta\% = \frac{R.hc}{q\lambda} \times 100 \tag{2.24}$$

where h is Planck's constant, c is the speed of light, λ is the incident light wavelength, and q is the electron charge.

2.7.3.3 Sensitivity

Sensitivity (S) of a photodetector is defined as the ratio of photocurrent to dark current as follows [107, 118]:

$$S = \frac{I_{ph}}{I_d} \tag{2.25}$$

where I_{ph} and I_d are the photo and dark currents, respectively.

2.7.3.4 Rise and Fall (Decay) Time

The speed of a photodetector is characterized by the rise time and the fall time of its response to an impulse signal. The rise time is defined as the rise in response time period from 10% to 90% of its peak value. The fall time is defined as the decay from 90% to 10% of its peak value. As shown in figure (2.6).

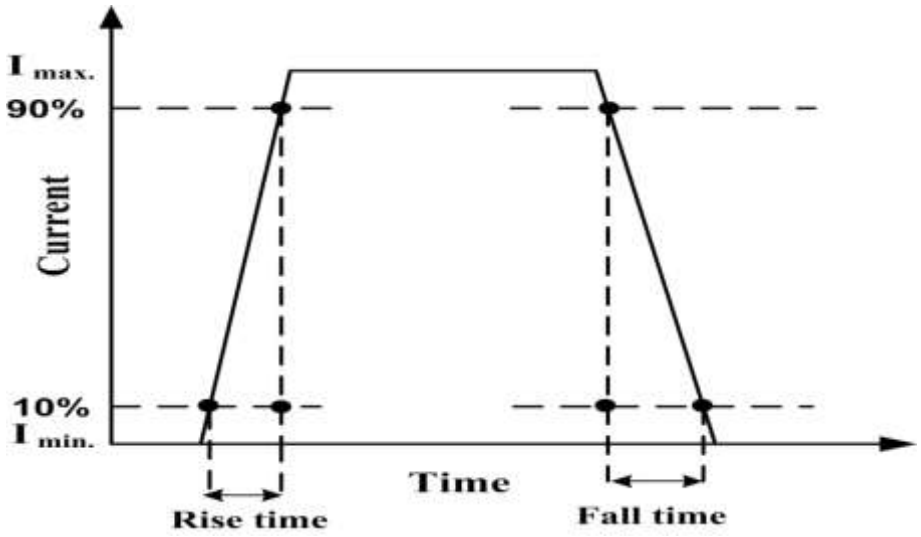

Figure 2.6 Calculation of: Rise time and fall time

CHAPTER 3: METHODOLOGY

3.1 Introduction

In this study, two methods of ZnO nanostructure synthesis were used. This chapter describes the methodology and instrumentation involved in these methods. The synthesis of ZnO nanostructures by PVD via VS and ECD techniques under different conditions is also discussed. The fabrication and characterization of MSM UV-PDs are investigated. The setting parameters, operating conditions, and the resolution of the instrumentations used to determine the factors involved are briefly described.

3.2 Synthesis of 1D ZnO by PVD Method in a Tube Furnace

3.2.1 Wafer Cleaning

The substrate should be properly cleaned to achieve intimate contact between a metal and a semiconductor. Wafer cleaning is a prerequisite of fabrication. In this study, the Radio Corporation of America (RCA) cleaning method was used to clean the Si samples. This method can be summarized in three steps.

In the first step, H_2O:H_2O:NH_4OH at a ratio of 5:1:1 was used at 80 °C for 10 min to remove insoluble organic contaminants. In the second step, HF:H_2O solution at a ratio of 1:50 was used to remove surface oxides. In the third step, H_2O: HCl: H_2O at a ratio of 6:1:1 was used at 80 °C for 10 min. The wafers were rinsed in deionized water and then dried under N_2 shower.